J. Fluid Mech. (2001), *vol.* 437, *pp.* 255–282. Printed in the United Kingdom

Experimental and theoretical study of shock wave propagation through double-bend ducts

By O. IGRA[1], X. WU[1], J. FALCOVITZ[2], T. MEGURO[3], K. TAKAYAMA[3] AND W. HEILIG[4]

[1]The Pearelstone Center for Aeronautical Engineering Studies, Department of Mechanical Engineering, Ben-Gurion University of the Negev, Beer-Sheva, Israel

[2]Institute of Mathematics, Hebrew University, Jerusalem, Israel

[3]Shock Wave Research Center, Institute of Fluid Science, Tohoku University, Sendai, Japan

[4]Ernst Mach Institute, Freiburg, Germany

(Received 25 May 2000 and in revised form 1 November 2000)

The complex flow and wave pattern following an initially planar shock wave transmitted through a double-bend duct is studied experimentally and theoretically/numerically. Several different double-bend duct geometries are investigated in order to assess their effects on the accompanying flow and shock wave attenuation while passing through these ducts. The effect of the duct wall roughness on the shock wave attenuation is also studied. The main flow diagnostic used in the experimental part is either an interferometric study or alternating shadow–schlieren diagnostics. The photos obtained provide a detailed description of the flow evolution inside the ducts investigated. Pressure measurements were also taken in some of the experiments. In the theoretical/numerical part the conservation equations for an inviscid, perfect gas were solved numerically. It is shown that the proposed physical model (Euler equations), which is solved by using the second-order-accurate, high-resolution GRP (generalized Riemann problem) scheme, can simulate such a complex, time-dependent process very accurately. Specifically, all wave patterns are numerically simulated throughout the entire interaction process. Excellent agreement is found between the numerical simulation and the experimental results. The efficiency of a double-bend duct in providing a shock wave attenuation is clearly demonstrated.

1. Introduction

Interactions between shock waves and structures have been the subject of numerous experimental and theoretical studies in recent decades, focusing on both understanding the basic physics of the flow field that develops and employing the accumulated knowledge for engineering treatment of explosion-related phenomena. When a planar shock wave propagates in a uniform-cross-section duct, it slowly attenuates due to momentum and energy loses via friction and heat transfer. A much faster decay in the shock wave strength and shape (pressure signature) is observed when it propagates into a bent duct. In this case the main mechanism responsible for reducing the shock wave strength, in addition to its diffraction over the bend corner, is multiple shock wave reflections initiated by the bending. Interest in shock wave propagation in ducts having bends or other complex geometry features has been stimulated not only by the theoretical background, such as the analysis of shock wave propagation, diffraction and reflection phenomena in ducts, but also by its

practical engineering applications. Some examples are: hazardous explosions in mine shafts or other industrial explosions; gas transmission pipes; exhaust systems of internal-combustion multi-cylindrical engines and in the design of shelters from bomb-generated explosions. Following such explosions, the effects of the air blast are typically transmitted to a large distance via shock wave propagation. A complex flow is generated behind the shock front due to multiple interactions between the transmitted shock wave and structures encountered by the shock. The propagation of a planar shock wave and its subsequent interactions with the duct walls, result in a highly non-stationary two-dimensional flow. In most of the above-mentioned examples, one is usually interested in quickly reducing the intensity (impulse) of the propagating shock, or blast, wave.

Studies published in the past three decades were limited to either experimental investigations or approximate theoretical/numerical solutions based on the assumption that the flow is quasi-one-dimensional. For example see Dekker & Male (1967), Dadone, Pandolfi & Tamanini (1971), Sloan & Nettleton (1971), and Heilig (1975). Approximating a non-steady flow in a duct of smoothly varying cross-section as quasi-one-dimensional may in some cases conform to the full two-dimensional solution; however, this is not so for every flow. For example, as shown in Igra, Wang & Falcovitz (1998), a simple rarefaction wave encountering an area convergence gives rise to an inherently two-dimensional flow, which even at late times differs from the corresponding one-dimensional solution. The flow in a double-bend duct considered herein is far more complex than that treated in Igra *et al.* (1998), and therefore it will certainly be wrong to treat it as a quasi-one-dimensional flow.

The present paper provides a comprehensive experimental and numerical study of shock wave propagation in several different double-bend ducts (Z-shaped tunnel) shown schematically in figure 1. Geometries similar to those shown are frequently used in underground shelters, with the aim of attenuating an explosion-generated blast wave before it enters the shelter interior. In order to assess the effects of the duct wall roughness on the strength and shape of the transmitted shock wave, one design was investigated with two alternative variants. The first is a duct having smooth walls (figure 1*a*), and the other has rough walls as shown in figure 1(*b*). For studying the effects associated with changes in the volume inside the double-bend duct on the flow developed behind the transmitted shock wave, geometries shown in figures 1(*c*) and 1(*d*) were investigated. The experimental part of the present study consists of either an interferometric or a shadowgraph/schlieren study of wave propagation into double-bend ducts. In the theoretical part, a two-dimensional numerical solution describing the flow field developed behind the transmitted shock wave is obtained.

2. Experimental set-up

Experiments using interferometric diagnostics were conducted in the 102 mm $\times$ 178 mm hypersonic shock tube of the Shock Wave Research Center, Institute of Fluid Science, Tohoku University, Japan. The models employed in these investigations are shown schematically in figures 1(*a*) and 1(*b*). In all experiments conducted with these geometries the test and the driving gases were nitrogen; the initial pressure and temperature in the shock tube driven section were 101.3 kPa and 294 K, respectively. The incident shock wave Mach number, prior to its impingement on the double-bend duct model, was $M_s = 1.2 \pm 0.5\%$. In the experimental work the incident shock wave Mach number was deduced by recording the time of arrival of the shock wave at two pressure transducers, each placed at a different point on the shock tube wall.

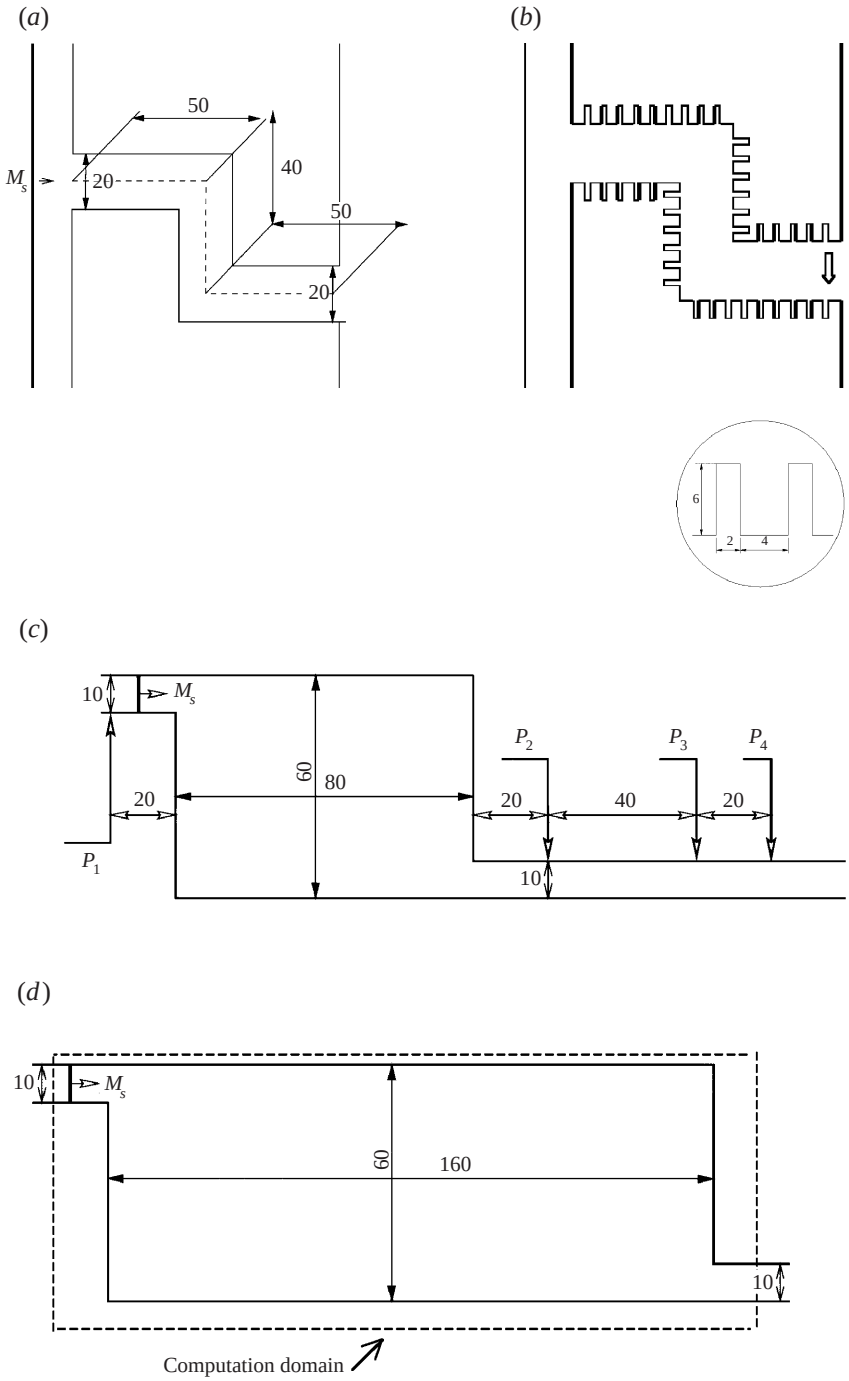

FIGURE 1. Schematic descriptions of the models investigated: (*a*) smooth-walled duct; (*b*) rough-walled duct; (*c*, *d*) geometries for the investigation of changes in volume inside the duct. Dimensions are in mm.

From the known distance between these pressure transducers and the measured time of arrival, the incident shock wave velocity is readily deduced. The shock wave Mach number is based on this velocity and the measured pre-shock gas temperature. It is probable that a small error might exist in the deduced Mach number. This is due to experimental errors and to shock wave attenuation between the place where the shock wave velocity was measured and the location of the shock tube test section, where the interferograms were taken. In the geometry to be investigated (figures 1*a* and 1*b*), a sequence of several interferograms was taken for quantitatively measuring the density fields and to record the history of a planar shock wave interaction with, and propagation into, the double-bend duct. In each experiment a single interferogram was taken at a pre-set time delay in order to cover the entire flow duration of about 1.4 ms.

Experiments with geometries shown in figures 1(*c*) and 1(*d*) were conducted in the 4 cm × 11 cm shock tube of the Ernst Mach Institute, Freiburg, Germany. In these experiments the flow field that developed inside the double-bend ducts was recorded by taking a sequence of alternating shadowgraph/schlieren photographs. A set of 24 photographs was taken at each shot covering the entire flow duration of about 1 ms. Details about the shock tube facility and the optical diagnostics used can be found in Mazor *et al.* (1992).

3. Numerical scheme

The time duration of the flows considered is less than 1.5 ms. In such short flow durations friction losses and heat transfer can safely be ignored in comparison with the on-coming flow momentum and energy. Therefore, in the present study, the gas flow can be modelled by the Euler equations, which express conservation of mass, momentum and energy for an inviscid compressible fluid obeying a perfect gas equation of state. For a two-dimensional, non-stationary flow the conservation equations, expressed in Cartesian coordinates, are

$$\frac{\partial}{\partial t}\boldsymbol{U} + \frac{\partial}{\partial x}F(\boldsymbol{U}) + \frac{\partial}{\partial y}G(\boldsymbol{U}) = 0 \tag{1a}$$

where

$$\boldsymbol{U} = \begin{bmatrix} \rho \\ \rho u \\ \rho v \\ \rho E \end{bmatrix}, \quad F(\boldsymbol{U}) = \begin{bmatrix} \rho u \\ \rho u^2 + p \\ \rho uv \\ (\rho E + p)u \end{bmatrix}, \quad G(\boldsymbol{U}) = \begin{bmatrix} \rho v \\ \rho uv \\ \rho v^2 + p \\ (\rho E + p)v \end{bmatrix}. \tag{1b}$$

$\boldsymbol{U}$ is the vector of unknown flow variables, $F(\boldsymbol{U})$ and $G(\boldsymbol{U})$ are the flux components in the x- and y-directions, respectively; p, ρ, u, v and E are pressure, density, (x, y) velocity components and total specific energy, respectively; x, y and t are Cartesian coordinates and time. A perfect gas equation of state is assumed, yielding

$$p = (\gamma - 1)\rho e, \quad E = e + (u^2 + v^2)/2, \tag{2}$$

where e is the specific internal energy and $\gamma > 1$; here γ is the constant specific heats ratio.

The finite-difference approximation to (1*a*) is formulated as a Strang-type operator splitting (Strang 1968), using the GRP (generalized Riemann problem) scheme as the one-dimensional finite-difference operator. The unique feature of the splitting procedure is preservation of second-order accuracy, i.e. as GRP is second-order

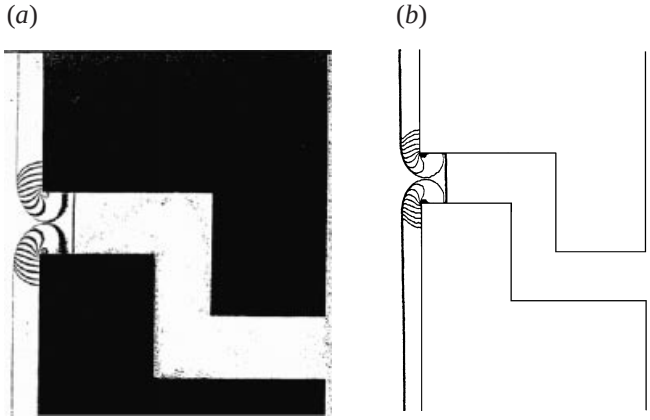

FIGURE 2. (*a*) Interferogram and (*b*) the corresponding simulation, showing the interaction of an initially planar shock wave with a double-bend duct, $t = 37.5\,\mu s$. Initial conditions are $P_1 = 101.3\,kPa$, $T_1 = 21°$, and $M_s = 1.2$.

accurate so is the two-dimensional conservation law scheme using GRP as its one-dimensional 'building block'. Details regarding the numerical scheme employed here are given in Igra *et al.* (1996).

4. Results and discussion

In results shown in figures 2 to 11 all experimental findings (part '*a*') are interferogram photos, and the corresponding numerical results (part '*b*') show lines of constant density. The computation domain is a rectangle 330 mm × 150 mm. In executing the numerical solution the flow field shown in figure 1(*a*) was divided into a grid of 990 × 450 square cells. Such a fine mesh ensures a high resolution in the numerical reconstruction of the flow field investigated. The time step is set equal to 0.333 μs, in compliance with the CFL stability condition.

In the following, most of the experimental results obtained (interferograms), along with their appropriate simulations, are shown. In figure 2, the wave pattern observed shortly after the incident shock wave arrives at the inlet to the double-bend duct is shown. It is apparent from figure 2(*a*) that part of the incident shock wave is reflected from the facing rigid wall, and the other part is transmitted into the duct. Both the reflected and transmitted waves are clearly visible in the interferogram and also in the simulation (figure 2*b*). The geometry and the location of both waves are perfectly reproduced in the numerical solution (figure 2*b*). It should be noted that in the simulation, thick lines represent surfaces through which discontinuous changes in density take place (shocks and/or contact surfaces); the thin lines are lines of constant density (isopycnics). Comparing figure 2(*a*) with figure 2(*b*), it is apparent that even the fringes shown in the interferogram are perfectly reconstructed in the simulation, both in shape and number of lines. The shock wave transmitted into the horizontal intake of the double-bend duct is planar and the flow behind it is subsonic. (As stated earlier, the incident shock wave Mach number is 1.2.) It will remain planar until it reaches the first expansion corner of the double-bend duct.

The flow developed in the double bend duct 100 μs later is shown in figure 3. The first stage of the interaction process in the bending segment is shown; as expected for a subsonic flow, the flow expansion over the 90° corner is via a vortex shed from the

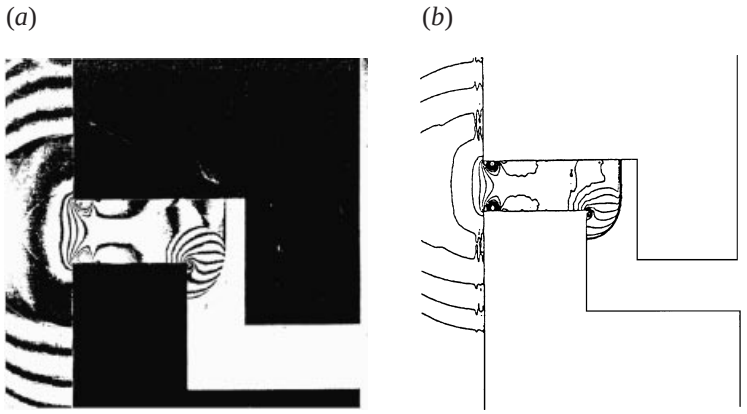

FIGURE 3. As figure 2 but at $t = 137\,\mu s$.

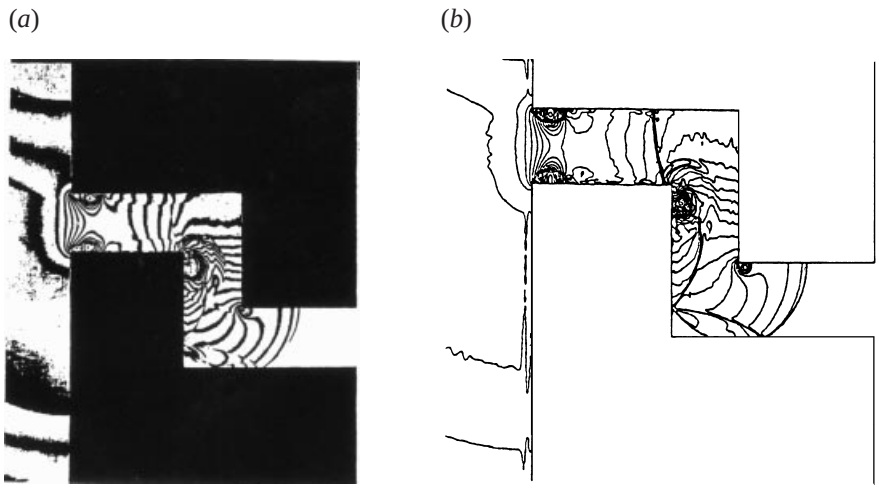

FIGURE 4. As figure 2 but at $t = 237\,\mu s$.

corner. The diffraction of the transmitted shock wave into the vertical section of the duct is clearly visible in figure 3. Owing to this diffraction the transmitted, initially planar shock wave, has evolved into a curved shock. Its upper part, which is normal to the horizontal wall of the duct, is stronger than its lower part, which diffracts around the corner into the vertical segment of the duct. This is typical for shock wave diffraction over an expansion corner, where the flow exhibits self-similarity (Igra *et al.* 1996). As observed for the earlier time, here too a near-prefect agreement is found between the interferogram (figure 3*a*) and its numerical simulation (figure 3*b*), regarding the wave shape and location, and fringes versus isopycnics. The flow near the inlet to the double-bend duct looks like a suction flow. It is accelerated via two vortices located just downstream of the duct inlet, producing a 'suction' effect in the flow field investigated. Outside the 'sucked flow pocket', seen in front of the duct inlet, the flow velocity is zero. This is expected for the flow behind a planar head-on reflected shock wave.

Until the transmitted shock wave (diffracting over the upper-left corner of the duct) hits, head-on, the right-hand wall in the vertical segment of the duct, the self-similarity

of the flow over the 90° expansion corner persists. This changes abruptly after the shock collides with the facing wall as is evident in figure 4(*a*), taken 100 μs after the event shown in figure 3. In figure 4(*a*) the following shock waves can be seen: The transmitted shock wave, which was originally a planar shock, is deformed into a weak curved shock wave (thin line). This shock is now seen in the lower horizontal segment of the duct. Before reaching this location it experienced a head-on collision with the wall of the vertical segment of the duct (right-hand wall), and the reflected shock wave propagates toward the other wall of the vertical segment of the duct (left-hand wall). This reflected shock wave is split into three different segments as is shown clearly in figure 4(*b*). The upper part, an upstream-facing shock wave, is propagating towards the duct inlet; the lower part hits the left-hand wall of the vertical segment of the duct and is reflected toward the opposite wall. This is clearly seen in both the interferogram and in its simulation. The central part interacts with the vortex shed from the first expansion corner inside the duct and engulfs the low-pressure zone around the vortex. This part of the reflected shock wave will cause splitting of the vortex, and is thereby significantly attenuated. Therefore, this shock is observed in figure 4(*b*) only as shifts in isopycnics and not as a dark solid line like the other two (stronger) parts of the reflected shock wave.

When comparing the interferogram (figure 4*a*) with its simulation (figure 4*b*), it is apparent that a good agreement exists between the two with respect to the waves and vortex pattern. The fact that the transmitted shock wave was significantly weakened during its propagation through the double-bend duct is shown in figure 4(*b*) by the thin line (weak) that represents it, in contrast to the thick line indicating the transmitted shock wave in figures 2(*b*) and 3(*b*). It should be noted that interferometry is much more sensitive in detecting small density changes than the present numerical solution; therefore the fringe counting and shape, although very similar, is not identical in figures 4(*a*) and 4(*b*). However, all major waves and vortices are accurately reproduced in the simulation.

At later times, multiple reflection from the duct walls and from collisions between reflected shock waves make the flow field highly non-steady, as shown in figure 5(*a*), which shows the flow field 100 μs after that in figure 4(*a*). Since the flow behind the transmitted shock wave is subsonic, the flow expansion over the duct lower right corner is also via a vortex shed from that corner. It is clear from figure 5(*a*) that the transmitted shock wave is a weak curved shock wave, the front of which has just emerged from the duct outlet. It will experience continued expansion outside the duct exit (the outflow), until the flow behind it reaches pressure equilibrium with the surrounding gas. As described while discussing figure 4(*a*), the upper part of the reflected shock wave continues propagating upstream towards the duct inlet. The central part of the reflected shock wave causes a splitting of the vortex: now two vortices are seen just downstream of the duct upper left corner. This central part of the reflected shock wave is weakened by its splitting collision with the vortex and can hardly be seen in figures 5(*a*) and 5(*b*). It is detectable in the enlargement of the flow field, near the upper left corner of the duct, shown in figure 5(*c*). There it appears as a weak compression wave engulfing the two vortices. It should be noted that a similar splitting of a corner-shed vortex by a shock wave, diffracting over a 90° corner, was also observed in Kliene, Ritzerfeld & Groenig (1995).

For evaluating the effect associated with the duct wall roughness, experiments and simulations made with the model shown in figure 1(*a*) were repeated with a similar double-bend duct, but equipped with 6 mm deep grooves as shown in figure 1(*b*). The initial flow conditions and the grid for the numerical solution are the same as

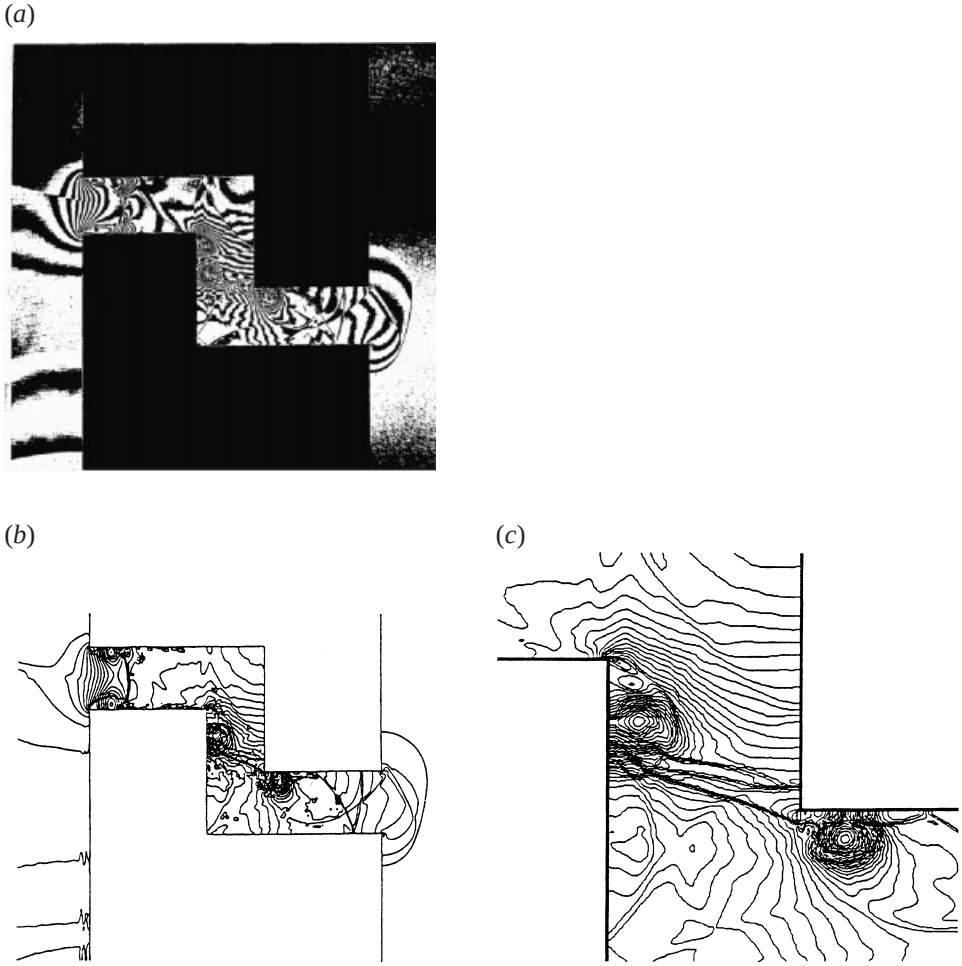

FIGURE 5. (*a*) Interferogram, (*b*) simulation, and (*c*) enlargement of a region near the upper-left corner of (*b*), showing the propagation of the transmitted shock wave inside the double-bend duct; $t = 337\,\mu s$.

those used previously for the geometry shown in figure 1(*a*). Similar results were obtained for an early time after the penetration of the transmitted shock wave into the duct inlet; see figures 2 and 6. A noticeable difference between the two figures is the appearance of expansion vortices, in figure 6, due to the flow expansion generated by the first, upper and lower, grooves downstream of the duct inlet. As could be expected, at later times a noticeable difference is observed between the two flows and wave patterns; compare figures 3 and 7. In the duct equipped with grooves (figure 7) the multiple shock reflections from all the grooves passed by the transmitted shock wave generate a complex, non-uniform flow field. In the interferogram shown in figure 7(*a*) multiple shocks and vortices are present. Some of them are so weak that they are not visible in the simulation given in figure 7(*b*). However, all major waves and vortices are visible in the simulation, such as the transmitted shock wave, shock waves reflected from the first few grooves, the two inlet vortices and the expansion vortex at the duct upper-left corner where the flow expands behind the diffracted shock wave.

(*a*) (*b*)

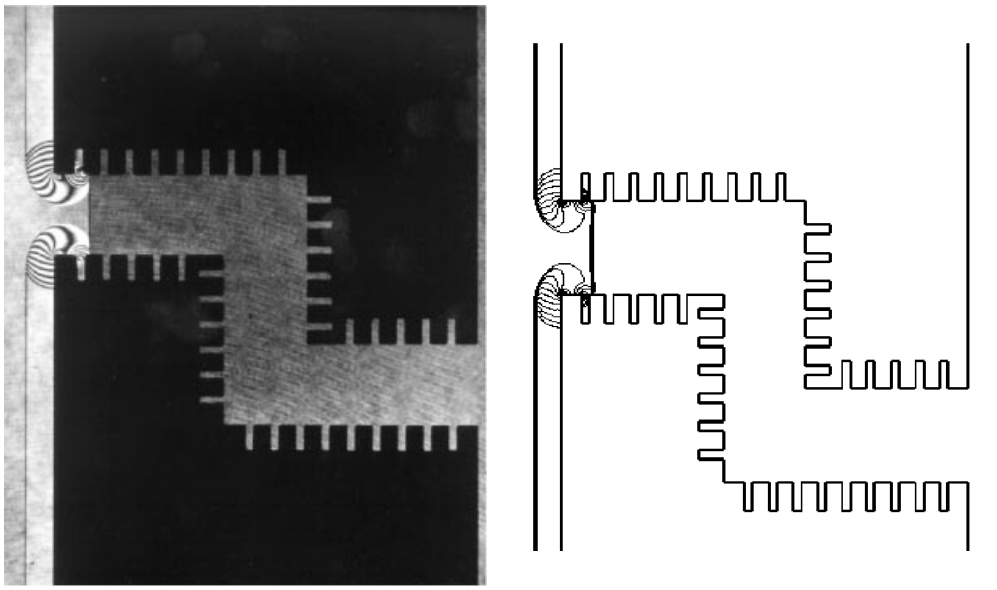

FIGURE 6. (*a*) Interferogram, (*b*) the corresponding simulation, showing the interaction of an initially planar shock wave with a rough-walled double-bend duct, $t = 37.5$ μs. Initial conditions as in figure 2.

The difference between the smooth and the very rough wall ducts becomes more pronounced as time passes, as is evident from comparing figure 4 with figure 8. Unlike the flow shown in figure 4, in figure 8 no quasi-uniform flow zone could be found. The transmitted shock wave is reduced now to a very weak wave; in the simulation (figure 8*b*) it appears as a Mach wave. In order to clearly demonstrate the strong effect that the wall roughness has on the transmitted shock wave, pressure signatures were computed at several points (mid-points) along the duct wall, and are shown in figure 9. It is clear from this figure that the pressure jump across the transmitted shock wave is significantly smaller in the case with very rough walls: about half the jump experienced in the smooth wall case. The fact that the highest first pressure jump is experienced at point P_2 is not surprising since there the transmitted shock wave is reflected, head-on, from the duct right-hand vertical wall.

Going back to figure 8, it is apparent that the simulation (figure 8*b*) reconstructs well all major waves appearing in the interferogram of figure 8(*a*). When comparing the rough wall case (figure 8) with the smooth wall case (figure 4) the differences; discussed above can be summarized as:

(i) The transmitted shock wave is weaker in the rough wall case. This is also evident from the transmitted shock wave position in the two figures. The stronger the shock, the faster it propagates inside the duct. It is evident that in figure 4 the transmitted shock wave is observed further downstream than in figure 8.

(ii) In figure 4 the interaction of the reflected shock wave (from the duct right-hand vertical wall) with the expansion vortex is clearly visible. The reflected wave is composed of three parts: one propagates upstream toward the duct's inlet, the second engulfs the vortex and the third hits and thereafter reflects from the duct left-hand vertical wall. A different wave pattern is observed in figure 8. Now three relatively

(*a*) (*b*)

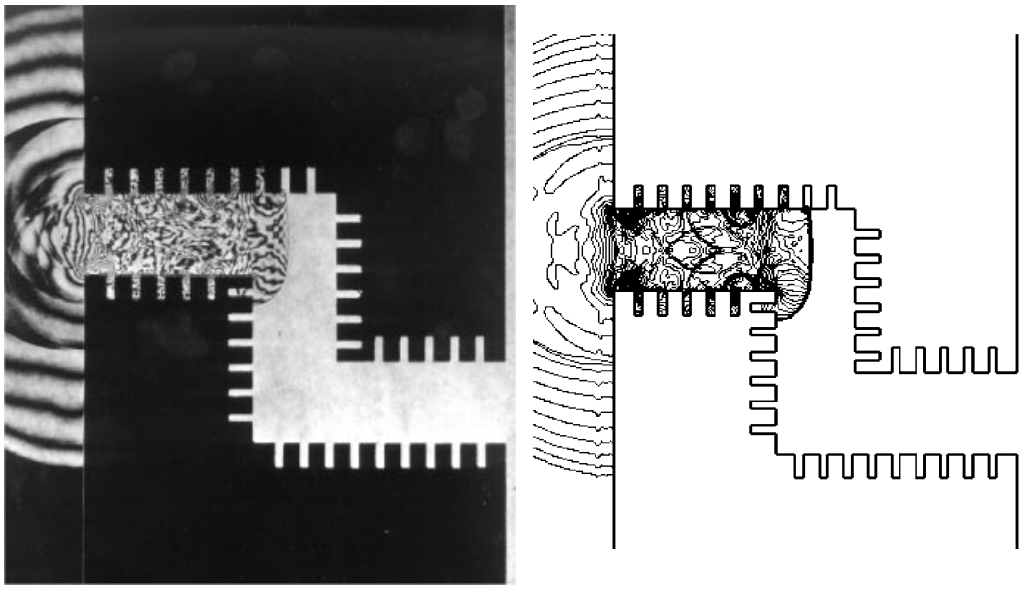

FIGURE 7. As figure 6 but at $t = 137\,\mu s$.

strong shock waves are present just downstream from the duct first expansion corner. The one nearest to the duct right-hand vertical wall is the primary reflection of the transmitted shock wave. It is an upstream-facing shock wave and it is followed by a secondary, wavy shock wave reflected from the bottom of grooves in the duct right-hand vertical wall. Since the primary reflected shock wave in the rough wall case is weaker than its counterpart in the smooth wall case, in its propagation upstream toward the duct inlet, it lags relative to its position in figure 4. Furthermore, in the rough case (figure 8) its lower part is so weak that it is hardly visible in figure 8(*b*). In figure 8(*a*) it is seen as a weak wave just touching the duct left-hand vertical wall. The third shock wave seen in figure 8, near the duct first expansion corner, results from coalescence of compression waves generated by reflections of the transmitted shock wave from passing the groove bottoms encountered along the duct walls. These compression waves can be seen in figure 7(*a*) prior to their coalescence to a shock wave.

To the inexperienced eye the three shock waves discussed above, appearing in figure 8, might be hard to detect. For clarity the computation was repeated for three simple geometries: one is a completely smooth wall duct terminated by an endwall; the second has the same geometry as the first with the exception that is *endwall* is grooved; in the third, *all* walls are grooved. The results obtained, shown in figure 8(*c*), clearly demonstrate the groove's effect on the wave pattern obtained. In the completely smooth wall case, shown at the top of figure 8(*c*), the expected single reflected shock wave is clearly observed. In the results obtained for a grooved endwall one easily detects two shocks. The first is the reflected shock wave from the groove frontal surface while the second is the wave reflected from the groove rear surface. The three shock waves mentioned while discussing figure 8(*a*) can also be detected in the lower part of figure 8(*c*); here all walls are grooved. As explained, the third shock wave results from the coalescence of compression waves generated by reflections of

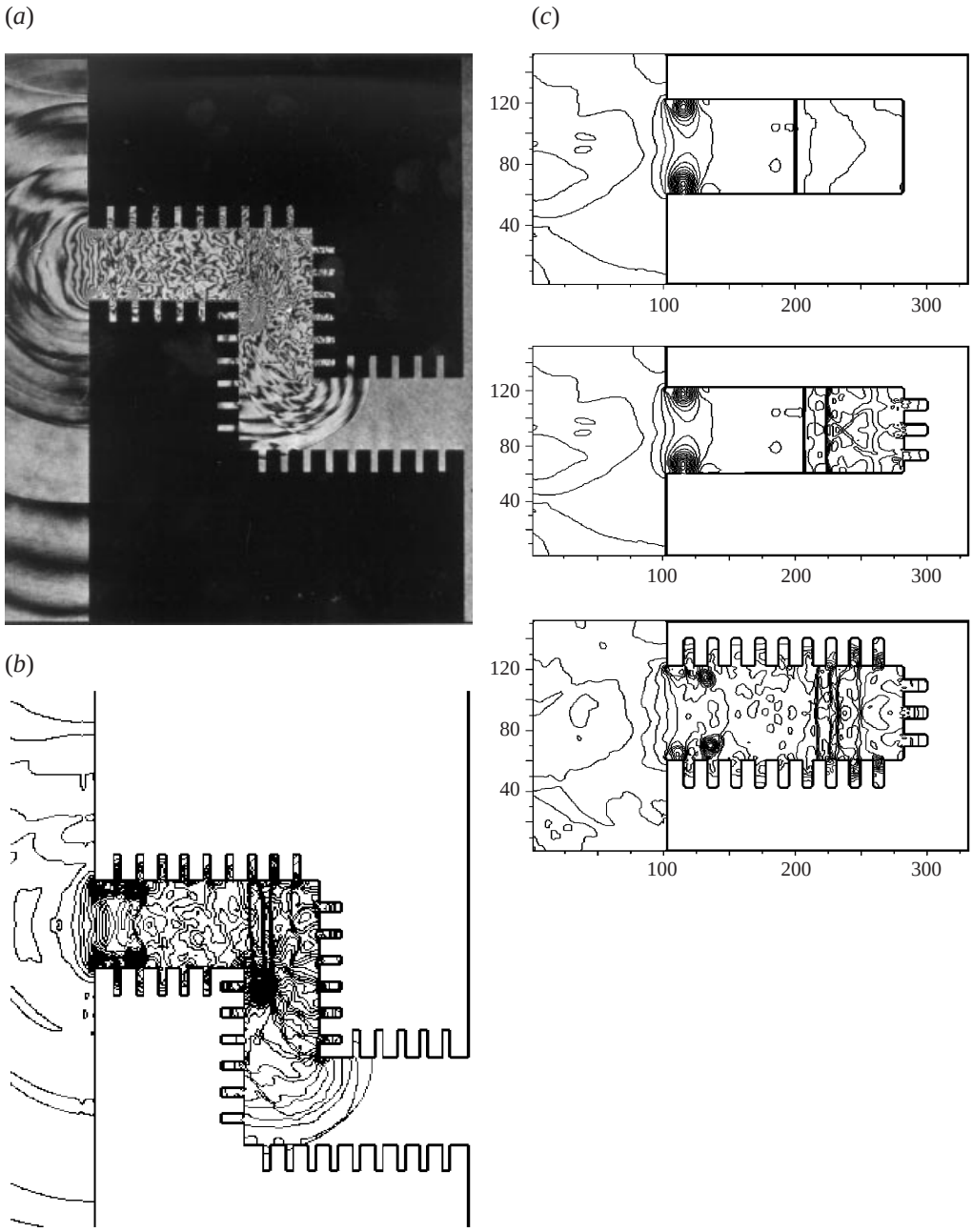

FIGURE 8. (*a*, *b*) As figure 6 but at $t = 236\,\mu$s. (*c*) Isopycnics showing the flow ahead of and behind a reflected shock from the duct endwall for three different duct wall surfaces. Initial conditions are $P_1 = 101.3$ kPa, $T_1 = 21°$, and $M_s = 1.2$.

the transmitted shock wave from passing the groove bottoms encountered along the duct top and bottom walls.

When comparing figure 5 with the corresponding rough-wall case (figure 10) it is apparent that in both cases the wave emerging from the duct outlet is a weak compression wave (Mach wave). The triple shock structure observed and discussed

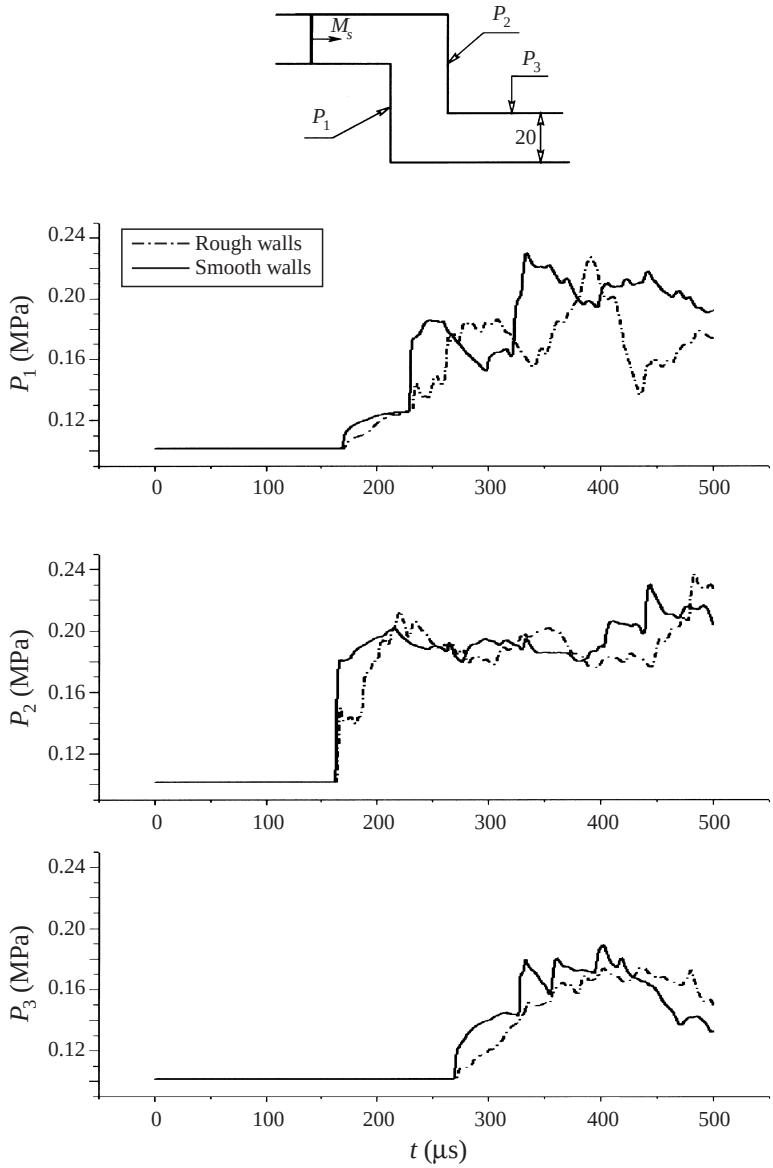

FIGURE 9. Calculated pressure histories at various positions along the duct wall.

in figure 8 appears in figure 10 as an upstream-facing, bifurcated shock wave. In the interferogram (figure 10*a*) this wave appears as thin lines between the 4th and the 5th grooves from the duct inlet. Primary vortices seen in figure 10(*a*) are reproduced correctly in the simulation (figure 10*b*). It is apparent from figures 10(*a*) and 10(*b*) that the flow in the last portion of the double-bend duct (the zone extending over the last three grooves of the duct) is much quieter than the upstream portion: almost a quasi-uniform flow. The double vortex observed in figure 5 and discussed earlier is also seen in figures 10(*a*) and 10(*b*). The last interferogram (figure 11*a*), taken 200 μs after that of figure 10(*a*), contains many vortices. The two appearing at the duct outlet are due to the subsonic flow expansion outside the duct exit plane. These are accurately

(*a*) (*b*)

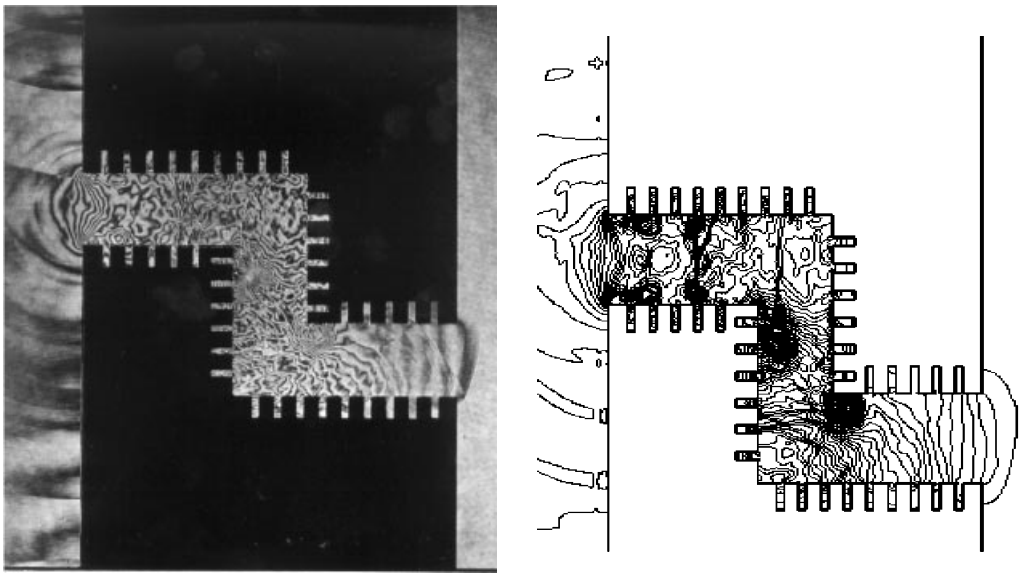

FIGURE 10. As figure 6 but at $t = 337\,\mu s$.

(*a*) (*b*)

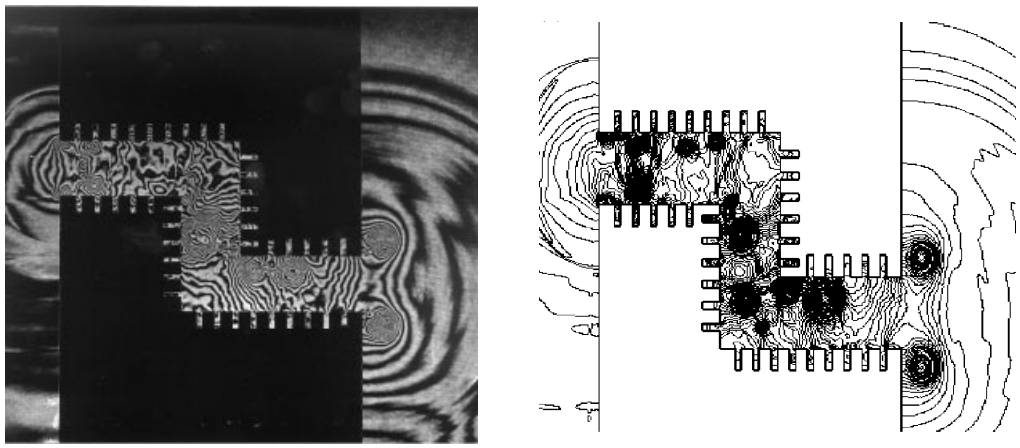

FIGURE 11. As figure 6 but at $t = 537\,\mu s$.

reproduced in the simulation shown in figure 11(*b*). The others, resulting from flow expansion over the two expansion corners of the duct and over corners produced by grooves placed along the duct wall make the duct flow highly non-uniform.

As mentioned in the Introduction, geometries like those shown in figures 1(*a*) and 1(*b*) could be useful for quickly attenuating shock and/or blast waves. In order to demonstrate and bring out their usefulness computations were repeated for four different geometries shown in figure 12. All four geometries have the same horizontal length and the same duct width. Pressure histories at two different location facing the duct exit were evaluated, for the following initial conditions: $P_0 = 1.1$ bar, $T_0 = 300\,K$

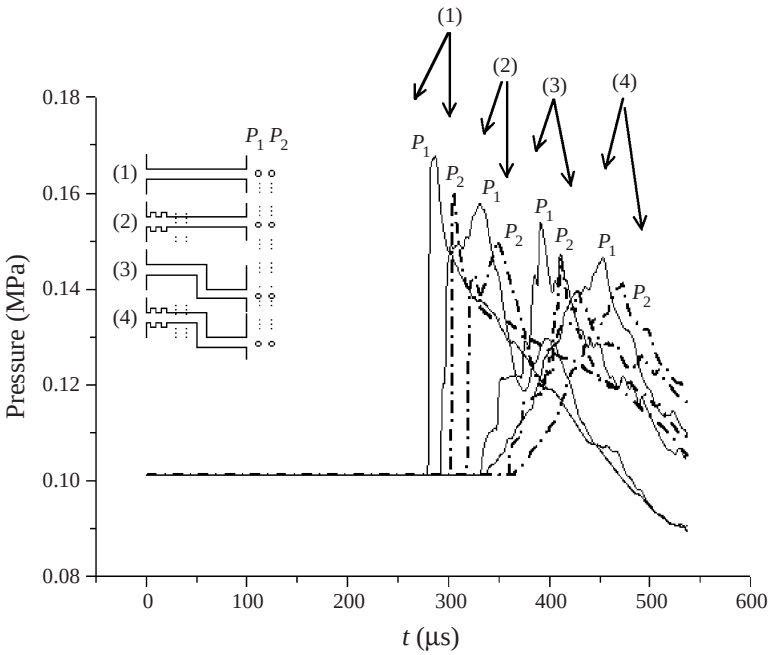

FIGURE 12. Calculated pressure histories at two different stations downstream of the duct exit plane, for four different geometries.

and $M_s = 1.2$. The first (at location marked P_1 in figure 12), is placed at a distance equal to one half of the duct width downstream from the duct's exit; the second, P_2 is at a distance equal to the duct width downstream from the duct exit plane. It is clear from the results shown in figure 12 that the highest pressure jump through the emerging shock wave is experienced in the case of a straight duct having smooth wall (case 1 in figure 12). A smaller jump is experienced when the straight duct has rough wall (case 2 in figure 12): a reduction of 15% in the maximum pressure obtained at P_1 and 19% for the maximum pressure obtained at P_2. In both cases the emerging wave has a clear shock wave signature, i.e. a sudden pressure jump. This is no longer the case when a double-bend duct is employed (cases 3 and 4 in figure 12). In the case of a smooth-wall double-bend duct (case 3) the emerging wave is a sequence of five weak shock/compression waves. As expected, the emerging wave strength decreases with increasing distance away from the duct outlet. Adding grooves to the double-bend duct (rough wall, case 4) significantly alters the pressure signature of the emerging wave. Now both waves (at P_1 and at P_2) are compression waves, and there are no sudden pressure jumps. In addition, the maximum pressure reached through these compression waves is 30% lower than that experienced in case 1; see figure 12. It may therefore be concluded that the combination of a double-bend duct with rough walls is an effective geometry for reducing a shock wave to a less harmful compression wave.

The optical diagnostics employed in experiments done with geometries shown in figures 1(*c*) and 1(*d*) were alternating shadowgraph and schlieren methods. Unlike the previously discussed cases, now a sequence of 24 frames of alternate shadowgraphs/schlieren photos were taken during *each* shot, covering a flow duration of about 600 μs. Simulations, which follow each shadowgraph/schlieren photograph, are results of a single computation sampled at the indicated time during the observed

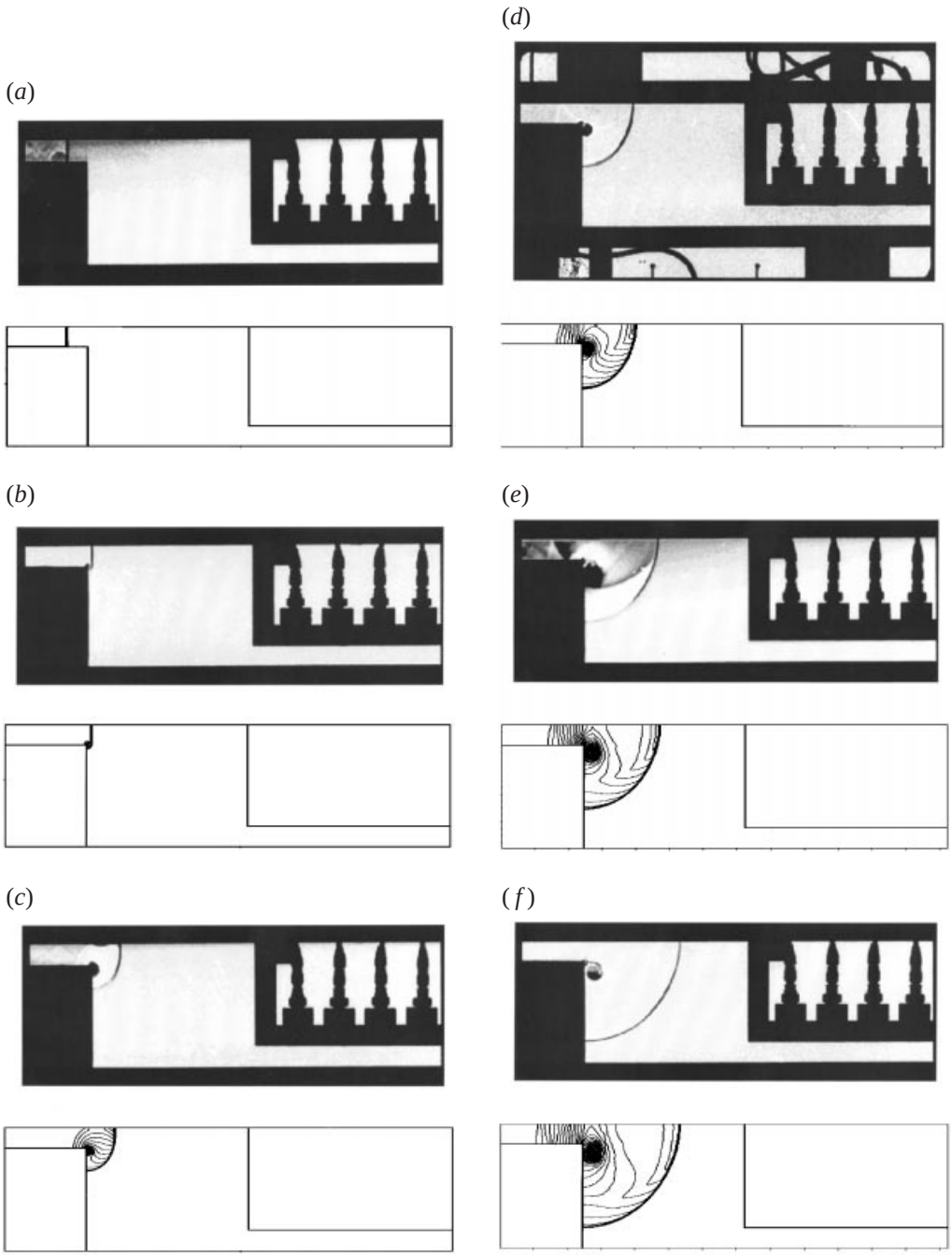

FIGURE 13(*a–f*). For caption see page 272.

flow. Since it is rare to have such a detailed experimental record of flow evolvement we believe it is worthwhile to show the complete set; furthermore, the very good agreement observed between experimental and numerical results for the *entire* flow duration attests to the reliability of the proposed physical model (equation (1)) and its numerical solution. The first set of results, which refers to the geometry shown

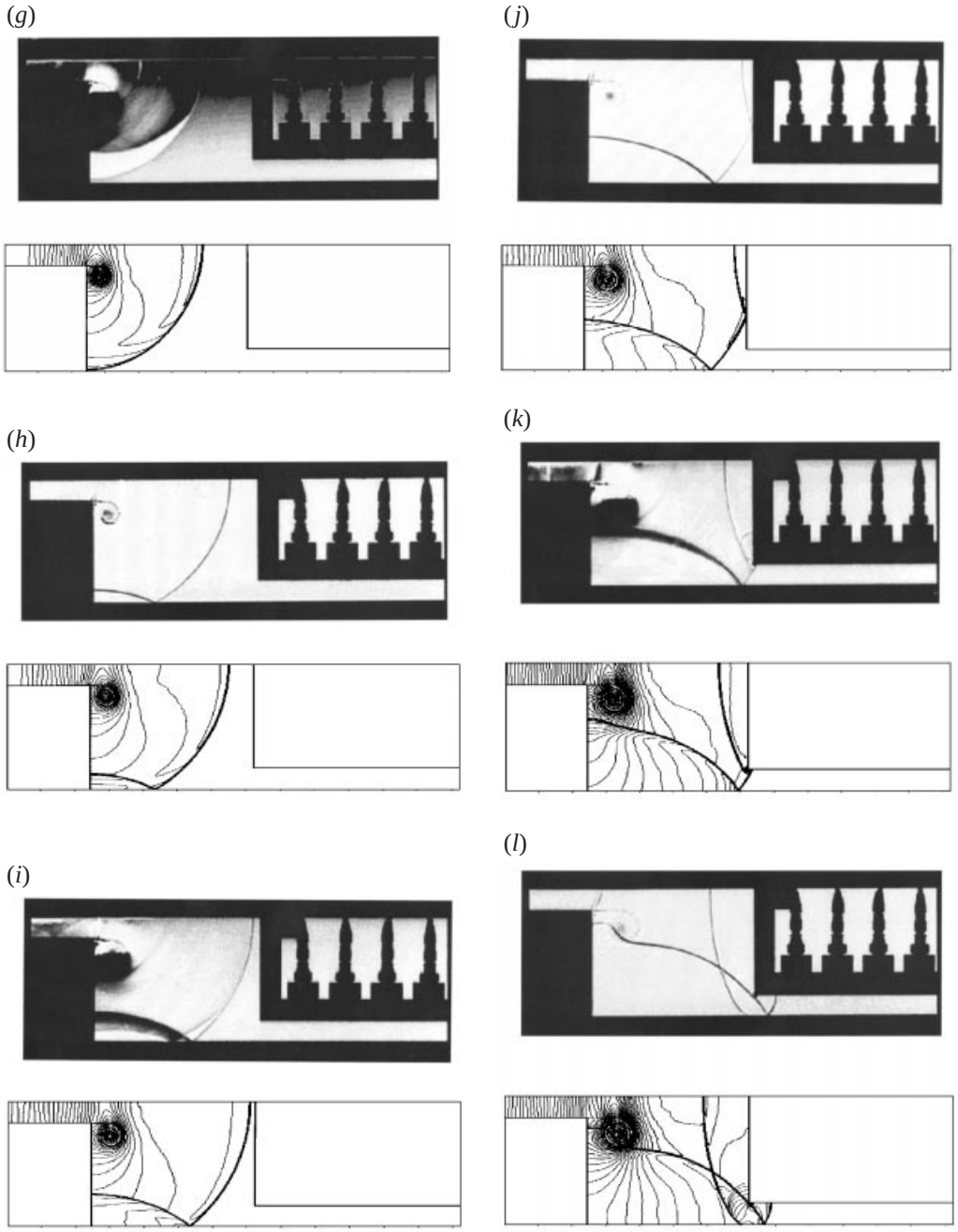

FIGURE 13(*g–l*). For caption see page 272.

in figure 1(*c*), is shown in figures 13(*a*) to 13(*w*), and was obtained for the following initial conditions: $P_1 = 0.987$ bar, $T_1 = 23.4\,^{\circ}\mathrm{C}$ and $M_s = 1.3466$. The geometry shown in figure 1(*c*) was divided into a grid of 660×180 square cells. As expected, until the diffracted shock wave hits the duct bottom wall (at $t \approx 175$ μs, figure 13*g*) the flow is essentially a shock wave diffraction over a 90° corner. Since the post-shock flow is subsonic the flow expansion is accompanied by a vortex shed from

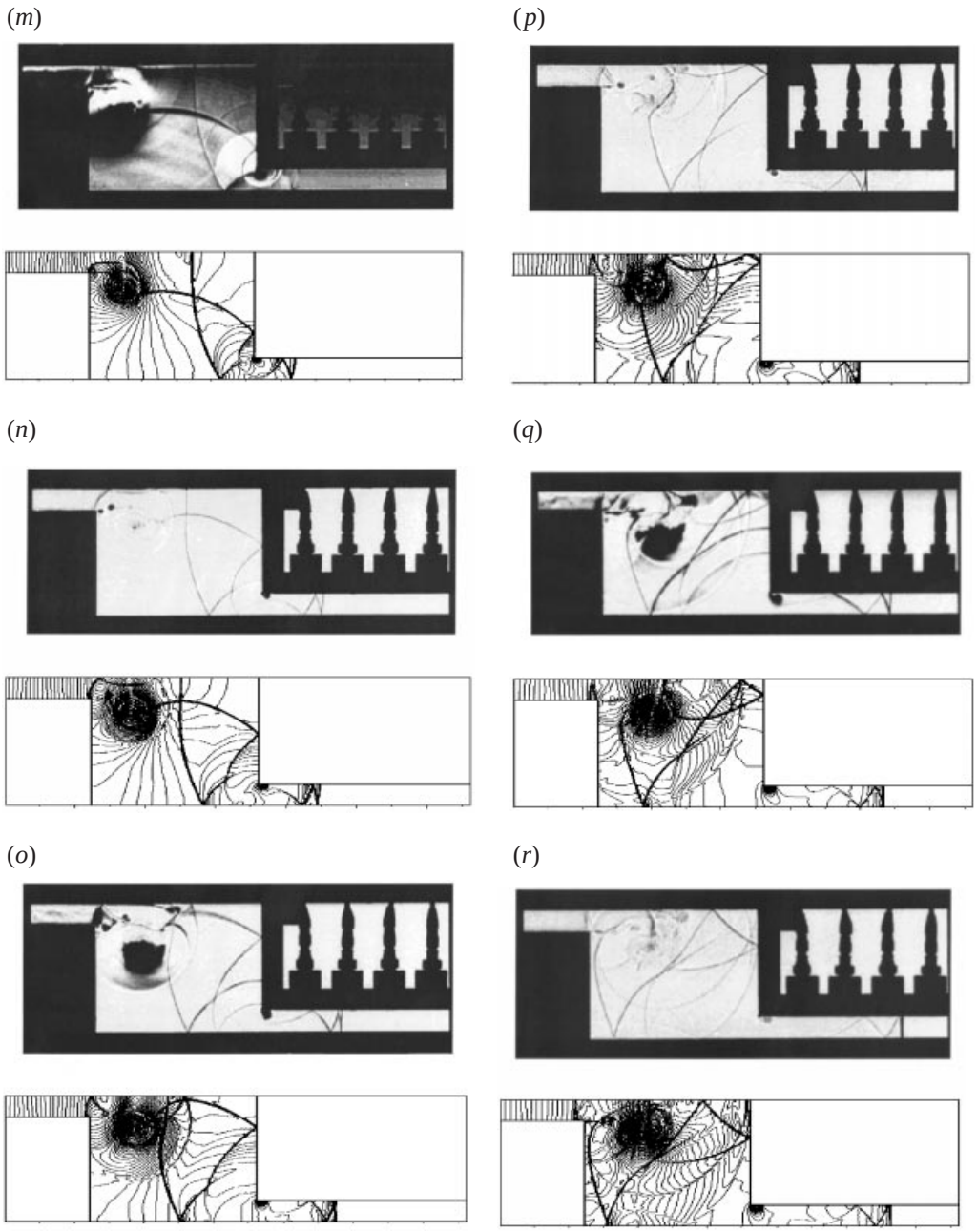

FIGURE 13(*m–r*). For caption see page 272.

the corner. Disturbances generated at the corner propagate both downstream and upstream.

It is clear from figures 13(*a*) to 13(*g*) that the numerical results reproduce accurately the experimentally observed wave pattern. The first collision of the diffracted shock wave with the duct walls is shown in figure 13(*h*) (with the bottom wall) and 50 μs later with the wall facing the transmitted shock wave; see figure 13(*j*). All shocks and the vortex shed from the duct upper-left corner are accurately replicated in the

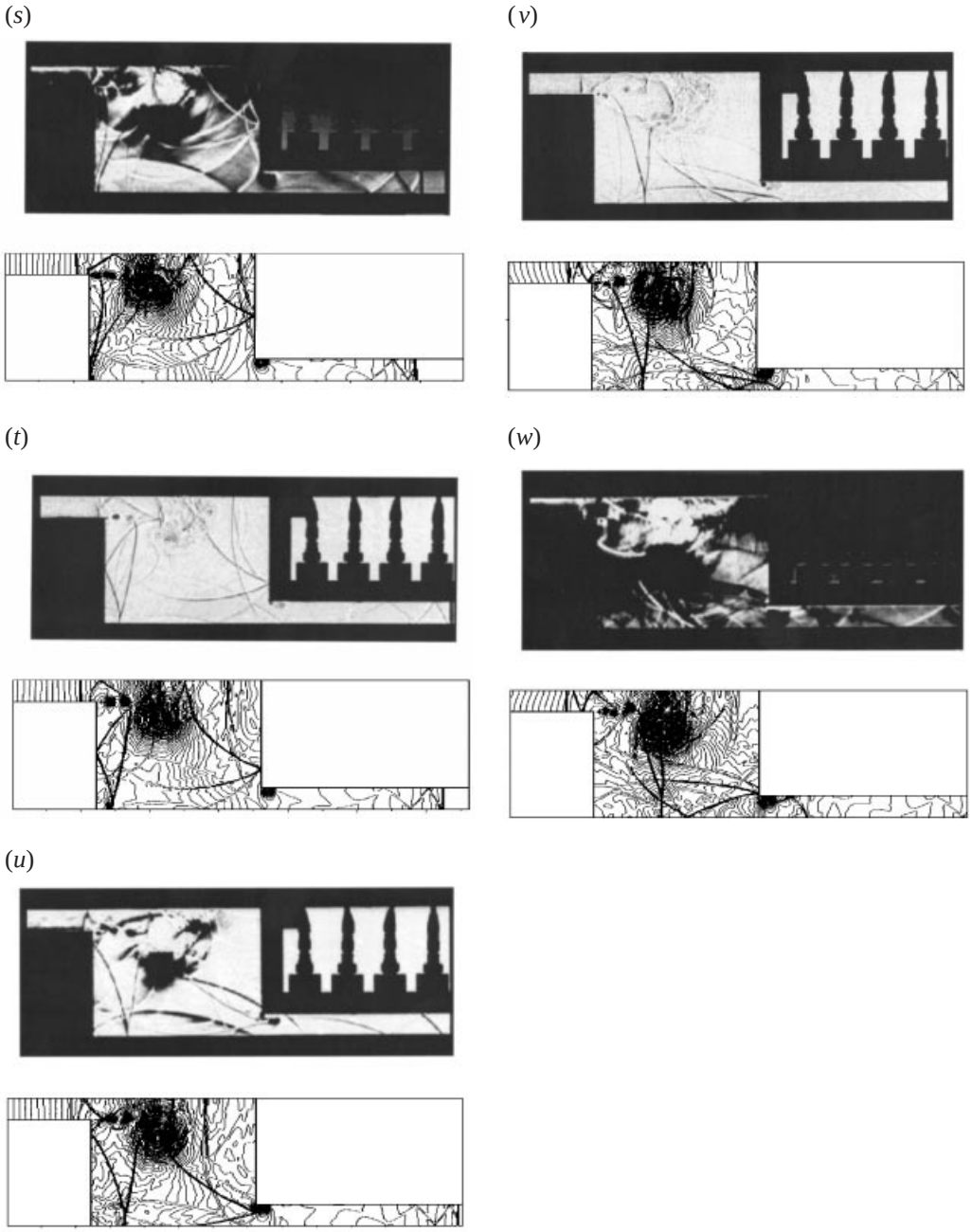

FIGURE 13. A sequence of 23 alternating schlieren (a, c, e, etc.) and shadowgraph (b, d, f, etc.) photographs (top) and corresponding simulations (bottom) showing the propagation of a shock wave inside the Z-tunnel shown in figure 1(c). Initial conditions are $P_1 = 0.987$ bar, $T_1 = 23.4°$, and $M_s = 1.3466$. (a) Wave pattern at $t = 25\,\mu s$, (b) 50 μs, (c) 75 μs, (d) 100 μs, (e) 125 μs, (f) 150 μs, (g) 175 μs, (h) 200 μs, (i) 225 μs, (j) 250 μs, (k) 275 μs, (l) 300 μs, (m) 325 μs, (n) 350 μs, (o) 375 μs, (p) 400 μs, (q) 425 μs, (r) 450 μs, (s) 475 μs, (t) 500 μs, (u) 525 μs, (v) 550 μs, (w) 575 μs.

simulations. As time progresses, multiple reflections from the duct walls and from collisions between reflected shock waves make the flow field highly non-steady in which no simple structure exists.

The transition from the nearly self-similar flow observed in figures 13(*b*) to 13(*g*) to the complex, highly time-dependent flow shown in figures 13(*m*) to 13(*w*) can easily be seen in figures 13(*h*) to 13(*l*). First, the diffracted shock wave is reflected from the duct bottom wall (figure 13*h*); 50 μs later three shock waves are present inside the duct. Moving from left to right in figure 13(*j*) one observes the reflected shock wave from the duct bottom wall, the part of the diffracted shock wave which propagates toward the lower horizontal channel of the double-bend duct, and the reflected shock wave from the duct right-hand vertical wall. An interesting wave pattern is observed in figure 13(*l*). Part of the original diffracted shock wave is now seen at the beginning (entrance) of the lower horizontal channel of the duct; it is followed by the shock reflected from the duct bottom wall. This reflected wave is propagating toward the duct upper wall; on its right-hand side it just reaches the duct lower expansion corner and on its left it interacts with the vortex shed from the duct upper expansion corner. Owing to this interaction it is weakened and experiences a change in its curvature, see figure 13(*l*). The shock wave reflected from the duct right-hand vertical wall continues its propagation toward the duct left-hand vertical wall and collides with the shock reflected from the duct bottom wall. Also observed in figure 13(*l*) is the beginning of an expansion vortex at the duct lower right-hand corner. At a later time, owing to multiple collisions between various shock waves and between shock waves and the duct walls, it is hard if not impossible to follow each wave. The resulting complex flow is shown in figures 13(*o*) to 13(*w*).

The flow in the lower horizontal part of the duct is initially unsteady and not uniform; see the curved shock at the entrance to the lower horizontal part of the duct in figure 13(*l*). As time passes, the curved shock becomes a planar shock wave followed by weak oblique shock waves (figures 13*r*, *s*, *t*). Later the oblique shocks reduces to Mach waves (figure 13*u*) and in the last figure (figure 13*w*) the approach to a uniform flow in the lower horizontal part of the duct is evident. However, the flow in the space between the two horizontal parts of the duct is still far from being steady or uniform.

It should be emphasized that throughout the flow duration investigated very good agreement is found between experimental findings (schlieren and shadowgraph) and the corresponding simulations. Obtaining good agreement between observed wave patterns in recorded schlieren or shadowgraph photographs and their numerical simulations is not a complete proof for the validity of the proposed physical model and its numerical solution. To enhance confidence in the accuracy of the present simulations, pressure measurement were recorded at the stations marked 1, 2, 3 and 4 in figure 1(*c*). (The location of these pressure gauges is also visible in shadow/schlieren photos shown in figure 13). Pressure histories were computed at these points using the GRP scheme, and the results are shown in figures 14(*a*) to 14(*d*). In figure 14(*a*) the pressure signature of the transmitted shock wave, before reaching the duct first expansive corner, is given. The expected shock wave signature is evident for the first 130 μs. That is, a sudden pressure jump (at $t = 0$) followed by a region of uniform high pressure. In the subsonic post-shock flow, pressure starts declining upon the arrival of disturbances (expansion) generated at the duct first expansive corner. The second (weaker) shock wave, clearly seen in the simulation at about 500 μs after termination of the uniform pressure zone, is due to the arrival of the upstream-facing shock wave at the recording point. This shock wave is apparent in figure 13(*u*).

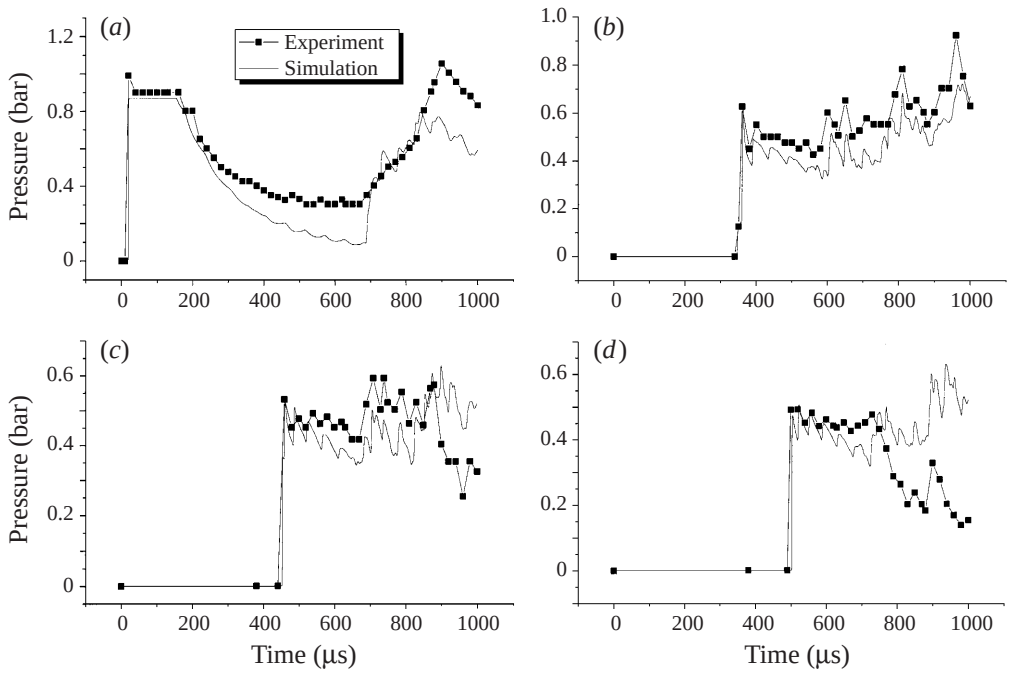

FIGURE 14. Pressure histories at (*a*) station 1, (*b*) station 2, (*c*) station 3, (*d*) station 4, of figure 1(*c*).

The discrepancy observed at late times between computed and recorded pressure is due to the following reason. As seen in the shadow/schlieren photos of figure 13 experiments were conducted inside a cookie-cutter inserted into the shock tube test section. At late times shock waves reflected from the cookie-cutter supports diffract into the double-bend duct investigated. Interference caused by these external waves is not included in the present computations.

Results shown in figure 14(*b*) indicate the pressure history at a station close to the second expansion corner of the duct; point 2 in figure 1(*c*). A clear pressure jump is seen upon the arrival of the transmitted shock wave at this position; a very short time after the event shown in figure 13(*l*). As could be expected this shock wave is attenuated while passing through the duct, and therefore the recorded pressure jump is smaller than that seen in figure 14(*a*). The wavy pressure history at point 2 is a result of the oblique shock wave structure which follows the transmitted shock; this wave pattern is seen in figures 13(*n*)–13(*t*).

Similar pressure histories are recorded/computed at positions 3 and 4 shown in figure 1(*c*); this is shown in figures 14(*c*) and 14(*d*), respectively. As expected, the further downstream the measuring station is, the lower is the pressure jump across the transmitted shock wave. Again, discrepancies observed at late times between computed and measured pressures are due to the exclusion of reflected shock waves from the cookie-cutter support structure in the present computation. It is apparent from figures 14(*a*) to 14(*d*) that very good agreement exists between the measured and the computed pressures until disturbances caused by shock reflections from the cookie-cutter support structure enter the flow field investigated. An additional reason for the observed discrepancies, primarily near the exit from the double-bend duct, is the fact that in the shock tube experiments the double-bend duct is a sub-insert in a broad test section and the flow around it affects the conditions (pressure) prevailing

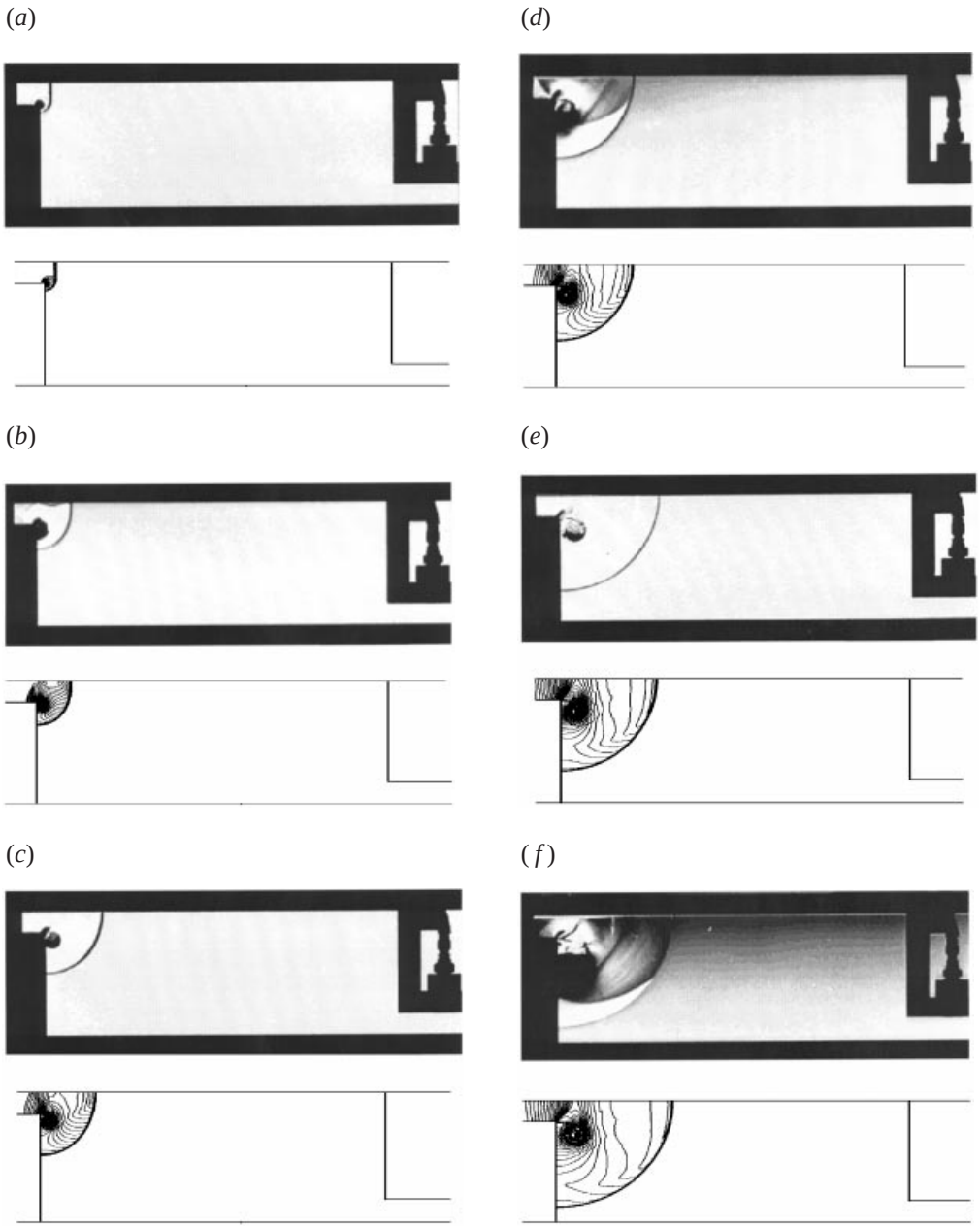

FIGURE 15(*a–f*). For caption see page 278.

near the exit of the double-bend duct. This effect is not included in the computational configuration.

It is also clear from results shown in figure 14 that the Z-tunnel investigated is effective in reducing the strength of the transmitted shock wave. While a pressure jump of about 0.9 bar is experienced behind the entering shock wave (figure 14*a*), the pressure jump behind the shock wave at station 4, in the duct outlet, is only about half of the entrance value. A similar behaviour was observed for the shock wave attenuation through the duct shown in figure 1(*a*); see figure 9.

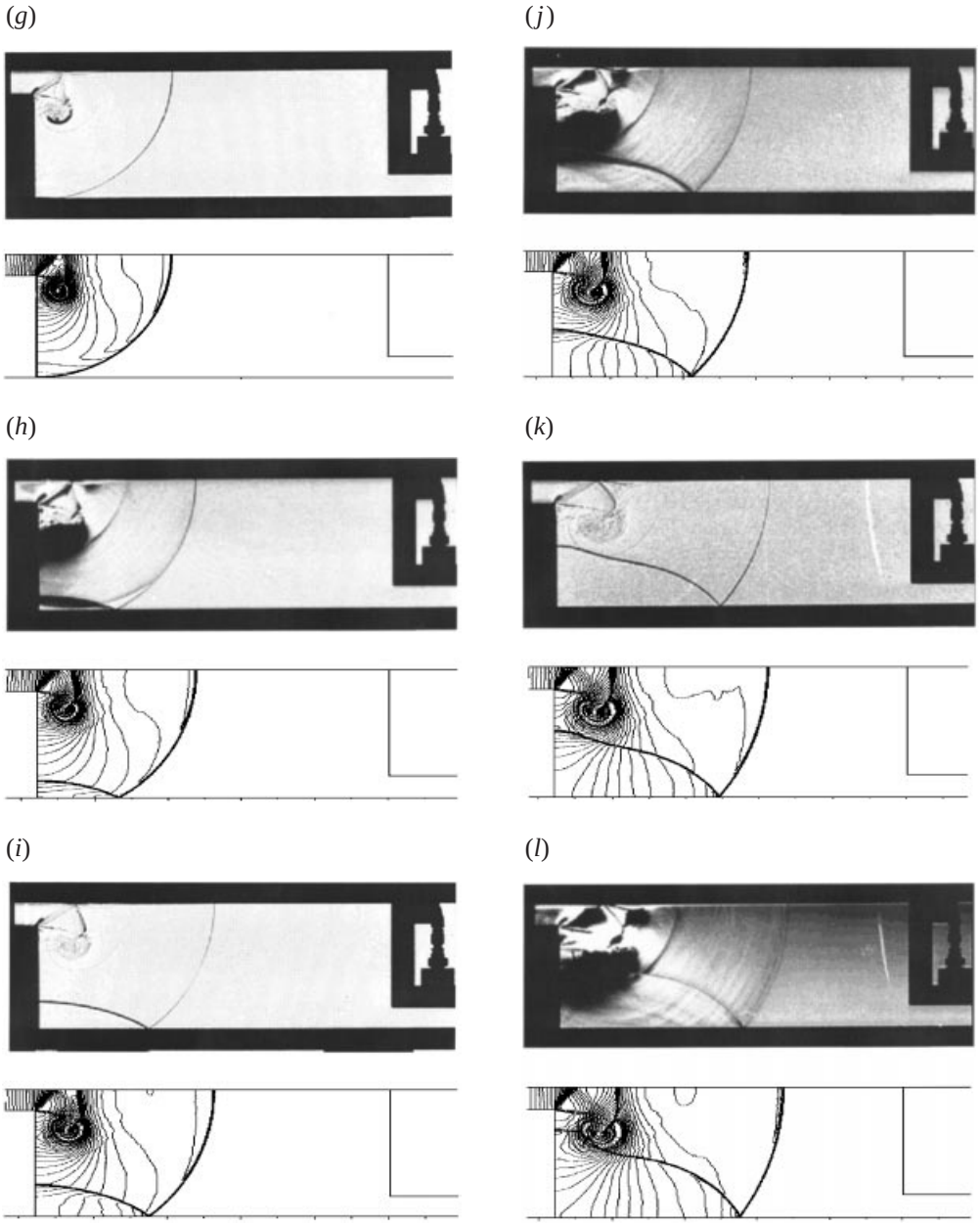

FIGURE 15(*g–l*). For caption see page 278.

The last duct geometry to be investigated is shown in figure 1(*d*). It was divided into a grid of 720×180 square cells. The experimental and numerical results obtained are given in figures 15(*a*) to 15(*v*). The flow inside this duct is similar to that observed for the duct shown in figure 1(*c*). The difference between the two cases is that the chamber in figure 1(*d*) is twice the length of that in figure 1(*c*). The initial conditions for the present case are: $P_1 = 0.982$ bar, $T_1 = 23.7\,^{\circ}$C and $M_s = 1.53$. Since we have a significantly longer duct now, the transmitted shock wave will be weaker when it approaches the exit of the double-bend duct. This weakening is manifested by a

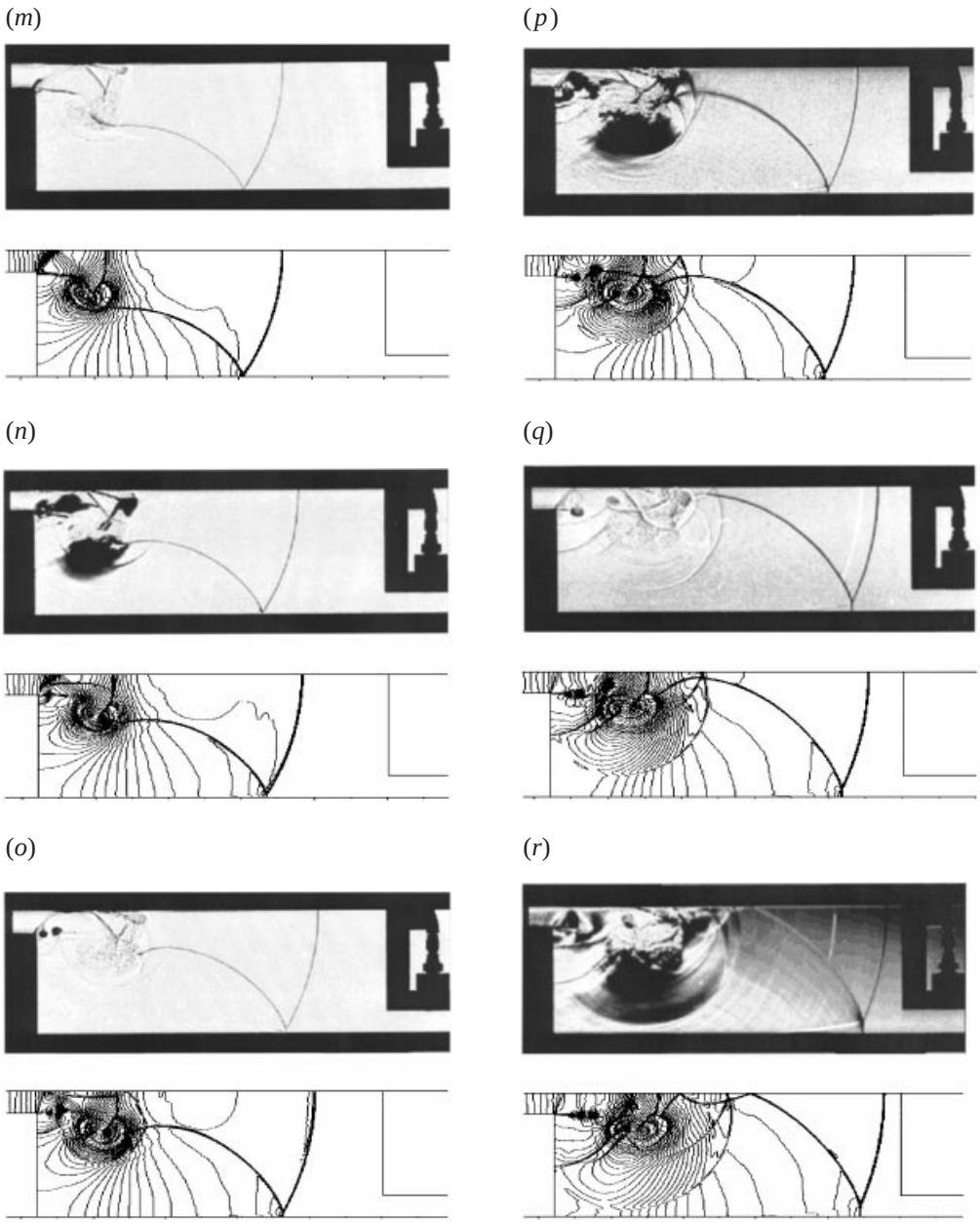

FIGURE 15(*m–r*). For caption see page 278.

change in the shock wave reflection from the duct bottom floor, from the regular reflection observed in the previous case (figures 13*h* to 13*l*), to a Mach reflection. In the present case, reflection of the transmitted shock wave from the duct bottom floor starts as a regular reflection (see figures 15*h* to 15*l*). The transmitted shock wave in figure 15(*l*) is located beyond the end of the duct chamber in the previous case (larger than 80 mm), and the shock wave Mach number at this location is appropriate to a maximum flow deflection angle. Further decrease in the shock wave Mach number results in a transition from regular to Mach reflection. This indeed

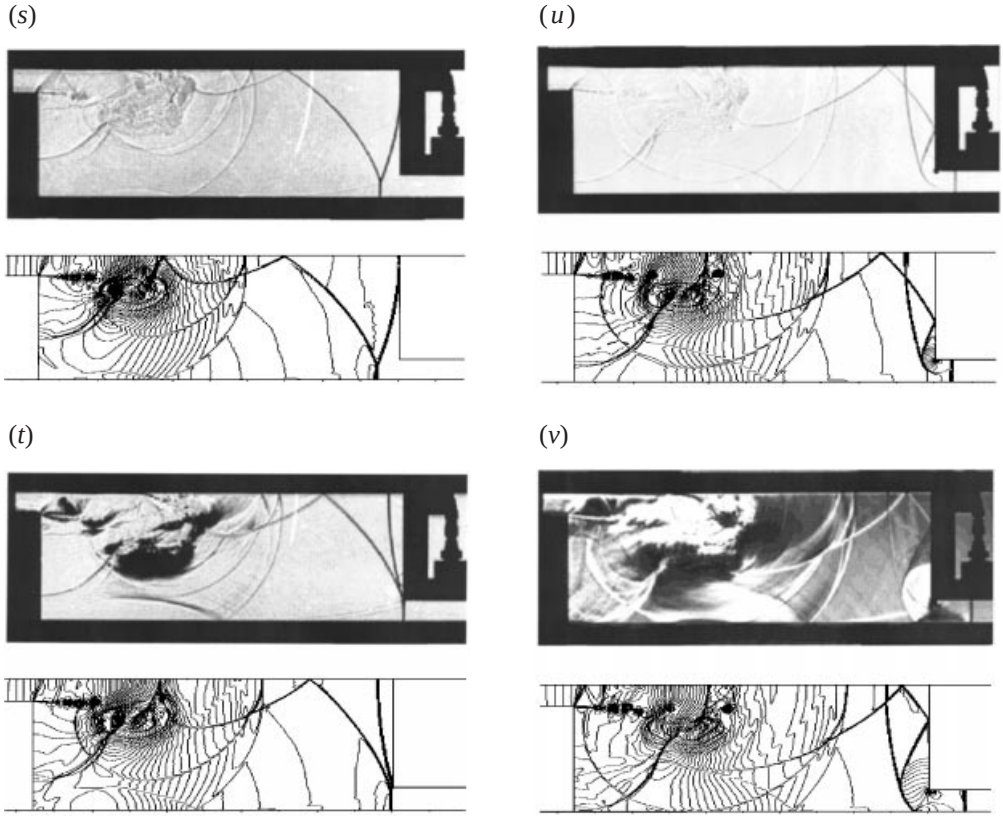

FIGURE 15. A sequence of 22 alternating shadowgraph (a, c, e, etc.) and schlieren b, d, f, etc.) photographs (top) and corresponding simulations (bottom) showing the propagation of a shock wave inside the Z-tunnel shown in figure 1(d). Initial conditions are $P_1 = 0.982$ bar, $T_1 = 23.7°$, and $M_s = 1.53$. (a) Wave pattern at $t = 20\,\mu$s, (b) 40 μs, (c) 60 μs, (d) 80 μs, (e) 100 μs, (f) 120 μs, (g) 140 μs, (h) 160 μs, (i) 180 μs, (j) 200 μs, (k) 220 μs, (l) 240 μs, (m) 260 μs, (n) 280 μs, (o) 300 μs, (p) 320 μs, (q) 340 μs, (r) 360 μs, (s) 380 μs, (t) 400 μs, (u) 420 μs, (v) 440 μs.

is the case, as is evident from figures 15(n) to 15(t). As could be expected, it is apparent from these figures that as time passes, the Mach stem size is increasing. The presence of a slipstream, starting from the triple point (where the three shock waves, the transmitted, the reflected and the Mach stem, meet) is clearly noticeable in figures 15(o) to 15(t). In the simulations it appears as a shift in the lines of constant density.

As observed in the previous case shown in figure 13, here too the flow starts as a nearly self-similar one; see figures 15(a) to 15(g). In figure 15(g) the transmitted shock wave is just hitting the duct bottom wall. In figure 15(h) the reflected shock wave is observed: it moves upward toward the duct upper wall. On its way it first interacts with the secondary, upstream-facing shock wave (figure 15k). This upstream-facing shock wave, which surrounds the vortex, is needed for matching the low-pressure zone generated by the vortex to the high-pressure zone prevailing behind the transmitted shock wave. This shock wave is first clearly observed in the shadowgraph shown in figure 15(e). In simulations its location is marked by shift in isopycnals. As a result of the interaction between the arch-shaped reflected shock wave and the secondary shock wave, the reflected shock wave experiences a change in its curvature; see figure 15(k).

As the reflected shock wave proceeds upward it collides with the corner shed vortex (figure 15*l*) and it experiences further bending. Eventually it splits into two segments as is evident from figure 15(*m*) on. The left-hand part, which moves faster due to the induced vortex flow, hits the duct upper wall first; its reflection from the upper wall is seen in figure 15(*o*). It takes a longer time for the right-hand part of the reflected shock wave to reach the duct upper wall; about 60 μs after the observed reflection of the left-hand part (figure 15*o*) the right-hand part is seen reflected from the duct upper wall, see figure 15(*r*). As time progresses, the flow becomes very complex and highly time dependent owing to multiple interactions between the various shock waves, the walls and the vortex. It should be emphasized again that throughout the flow duration very good agreement is found between experimental findings and their simulations regarding the wave pattern, location and geometry, lending credibility to the proposed physical model and its numerical simulation.

Owing to multiple interactions between various reflected shock waves and the vortex shed from the duct left-hand corner, the vortex is distorted (figure 15*m*) and thereafter splits to several vortices (figures 15*o* and 15*q*). As time progresses these vortices spread in a pattern reminiscent of the classical von Kármán vortex street (see figures 15*u* and 15*v*).

It is clear from the discussion regarding the flow and wave pattern evolving inside a double-bend duct (like the geometries shown in figure 1), that the volume of the intermediate double-bend space has a significant effect on the magnitude of the pressure jump across the diffracting/transmitted shock wave. Increasing the volume of the expansion chamber inside the double-bend duct also reduces the strength of the transmitted shock wave. The reason for this is that the longer the chamber is, the weaker is the transmitted shock wave diffracting over the first 90° expansion corner of the ducts considered.

An optimum in the shock attenuation obtained exists since, once the diffracted shock wave is reflected from the chamber bottom wall, the weakening diffraction process is terminated. In order to clearly illustrate this effect, comparative computations were performed for seven different double-bend duct geometries. The parameter changed was the ratio between the duct chamber length (L) and its horizontal conduit height (H); see the sketch in figure 16. Computations were conducted for $L/H = 1, 2, 3, 4, 6, 8$ and 16. In all computations the following initial conditions were employed: $P_1 = 0.987$ bar, $T_1 = 23.4\,^{\circ}\mathrm{C}$ and $M_s = 1.3466$. Results obtained for pressure histories at three stations in the lower horizontal part of the double-bend duct are shown in figure 16. It is clear from these results that the intermediate double-bend volume has a distinct effect on the pressure histories of the transmitted shock. For $L/H = 1$ and 2 the difference in the post-shock pressure obtained is very small (see figure 16). For $L/H = 3$ it is clear that the first pressure jump is smaller than in the previous cases; however the magnitude of the maximum attained pressure is very similar to that obtained for $L/H = 1$ or $L/H = 2$. A clear change in the pressure history is evident when $L/H = 4$. Now the maximum pressure jump across the transmitted shock wave decreases to about one half of what it was in cases with $L/H = 1$, 2 or 3; see figure 16. This indicates that the transmitted shock wave is attenuated faster when it expands into a duct having a larger chamber space. The second pressure jump is also lower now, indicating that the reflected shock wave is also weaker in the present case.

Another interesting phenomenon seen in figure 16 is that for $L/H \geqslant 4$, the first pressure jump, across the transmitted shock wave, is almost independent of L/H. This leads to the conclusion that there exists a critical value of L/H which controls

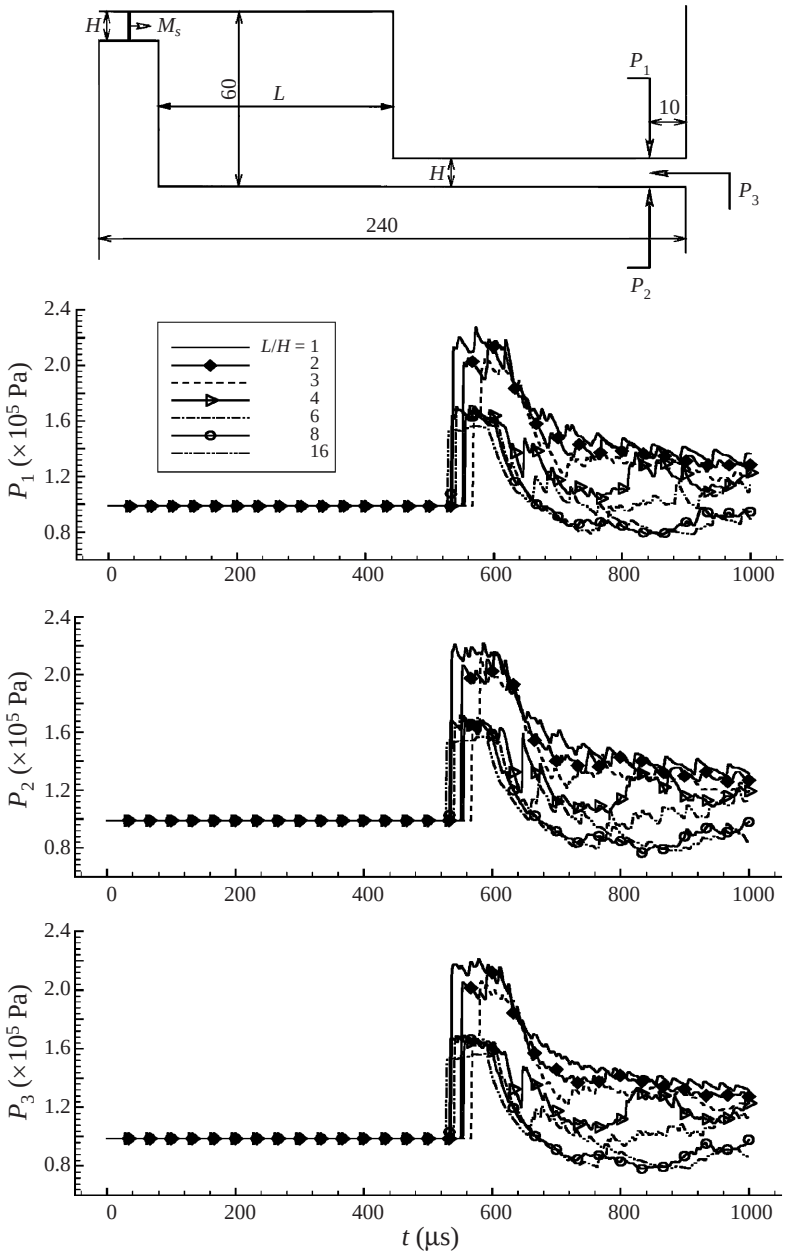

FIGURE 16. Computed pressure histories at three points for double-bend ducts with different intermediate spacing L.

the strength of the transmitted shock wave. This conclusion is clearly verified from figure 17 where the peak pressure obtained behind the shock front is presented as function of L/H. The pressures shown were computed at point P_3 of the sketch in figure 16. It is apparent from figure 17 that only a small decrease in pressure is associated with increasing L/H within the range $1 < L/H < 3$. A large decrease in pressure is observed when L/H is increased from 3 to 4. Thereafter, further increase in L/H results in only a mild decrease in the post-shock pressure. This indicates that

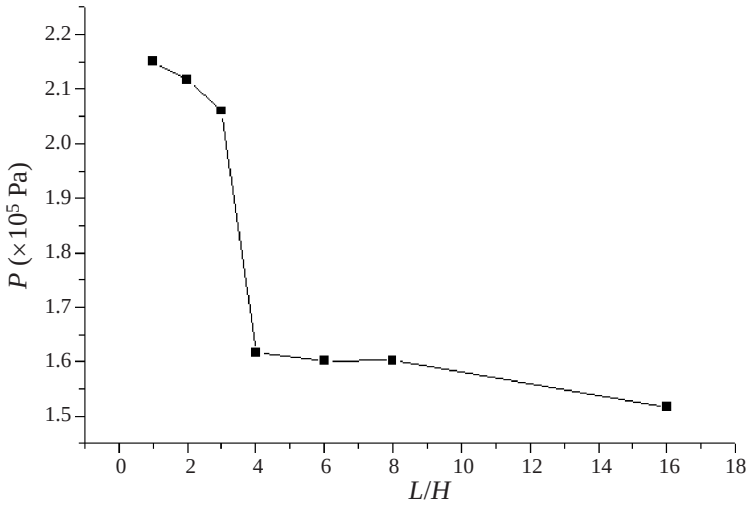

FIGURE 17. Peak pressure behind the transmitted shock waves versus L/H.

for efficient shock attenuation by the double-bend duct considered an intermediate spacing of $L/H = 4$ should be used (for incident shock wave Mach number of 1.35).

It should be noted that although real fluids are viscous, and our theoretical model assumes an inviscid fluid, the numerical simulations exhibit corner-shed vortices akin to those observed in experiments. The 'inviscid' mechanism by which these vortices are generated is the strongly rotational flow generated by the curved shock wave resulting from the expansive diffraction of the transmitted shock wave over the upper-left and the lower-right corners of the duct. Apparently, at early times this mechanism is the dominant one and lack of viscosity does not significantly alter the vortex formation. Note however, that this argument is valid with respect to an analytic solution of the Euler equations describing the corner shock diffraction. In the numerical solution, truncation errors invariably give rise to a 'numerical viscosity', so that strictly speaking, the numerical solution is never perfectly inviscid. Just the same, no wall friction is present, so that with respect to the vortex shedding process, vorticity is generated by the 'inviscid mechanism' previously described, and the wall boundary layer is absent.

5. Concluding remarks

The flow field and wave pattern resulting from the propagation of an initially planar shock wave through various double-bend ducts was studied experimentally and theoretically/numerically. The experimental study includes optical diagnostics (interferogram, schlieren and shadowgraph techniques) and pressure measurements. In the theoretical part, the flow was assumed to be governed by the conservation laws for a perfect, inviscid gas. Such a physical model is suitable for describing shock waves propagation through non-regular ducts (like the double-bend duct considered), at early times, before a steady flow is reached. For such short flow durations viscous and heat transfer losses have a negligibly small effect on the flow. The numerical scheme used for solving the proposed physical model, the GRP, provides a very accurate simulation of the observed complex flow field throughout the flow duration investigated.

It was shown that double-bend duct geometry is effective in obtaining a quick attenuation of the shock wave transmitted through it. Furthermore, there is a critical value of L/H for which fast wave attenuation is obtained, which in the present case was found at $L/H = 4$. For ratios above and/or below this critical value, changes in pressure jump across the transmitted shock wave front associated with changes in L/H are small.

Adding roughness to the duct wall further reduces the pressure jump across the transmitted shock wave.

The excellent agreement observed between experimental results and the GRP simulations provides evidence of the accuracy of the proposed physical model and its numerical solution. It could therefore be safely used for other shock-wave-generated flow fields.

REFERENCES

Dadone, A., Pandolfi, M. & Tamanini, F. 1971 Shock waves propagating in a straight duct with a side branch. In *Shock Tube Research* (ed. J. L. Stollery, A. G. Gaydon & P. R. Owen), pp. 17/1–17/13. Chapman & Hall.

Dekker, B. E. L. & Male, D. M. 1967 Fluid dynamic aspects of unsteady flow in a branched duct. *Thermodynamics and Fluid Mechanics Conversion, Proc. I. Mech. Eng.* **182**, (Pt 3H), p. 167.

Heilig, W. 1975 Propagation of shock waves in various branched ducts. In *Modern Developments in Shock Tube Research* (ed. G. Kamimoto), pp. 273–283. Shock Tube Research Society, Japan.

Igra, O., Falcovitz, J., Reichenbach, H., & Heilig, W. 1996 Experimental and numerical study of the interaction between a planar shock wave and a square cavity, *J. Fluid Mech.* **313**, 105–130.

Igra, O., Wang, L. & Falcovitz, J. 1998 Non-stationary compressible flow in ducts with varying cross-section. *Proc. Inst. Mech. Engrs* G **212**, 225–243.

Kliene, H., Ritzerfeld, E., & Groenig, H. 1995 Shock wave diffraction – new aspects of an old problem. In *Proc. 19th Intl Symp. On Shock Waves, Marseille, France*, Vol. IV (ed. R. Brun & L. Z. Dumitrescu).

Mazor, G., Igra, O., Ben-Dor, G., Mond, M. & Reichenbach, H. 1992 Head-on collision of normal shock waves with a rubber-supported wall. *Phil. Trans. R. Soc. Lond.* A **338**, 237–269.

Sloan, S. A. & Nettelton, M. A. 1971 The propagation of weak shock waves through junctions. In *Shock Tube Research* (ed. J. L. Stollery, A. G. Gaydon & P. R. Owen), pp. 18/1–18/14. Chapman & Hall.

Strang, G. 1968 On the construction and comparison of difference schemes. *SIAM J. Numer. Anal.* **5**, 506–517.